EFFECTS OF ELASTIC PILLARS ON FLUID-FLOW AND HEAT TRANSFER ENHANCEMEN IN A MICRO-CHANNEL

by

Mingzheng YE[a], Xian YANG[a], Jin WANG[a*], Milan VUJANOVIC[b], and Bengt SUNDEN[c]

[a] School of Energy and Environmental Engineering, Hebei University of Technology, Tianjin, China
[b] Department of Energy, Power Engineering and Environment, Faculty of Mechanical Engineering and Naval Architecture, University of Zagreb, Zagreb, Croatia
[c] Department of Energy Sciences, Division of Heat Transfer, Lund University, Lund, Sweden

Original scientific paper
https://doi.org/10.2298/TSCI220617139Y

In this paper, periodic vortices are generated by a fluid passing a cylindrical obstacle, d, near the micro-channel inlet. Two elastic pillars are arranged on the walls, and the effect of the pillar spacing on heat transfer performance is studied using the Arbitrary Lagrangian-Euler method. With the spacing of 10d, the small pillar amplitude of 2 μm is not conducive to the generation of vortices. The flexible vortex generator has higher heat transfer efficiency and lower pressure loss than the rigid vortex generator. The two pillars with no spacing generate isolated vortices, and the mixing of these vortices is insufficient downstream the pillars. It is found that with the pillar spacing of 5d, the overall performance factor is significantly higher than that with the pillar spacing of 0d and 10d in the Reynolds number range of 800 to 1100. The average Nusselt number with the spacing of 5d increases by 19.2% compared to that with the spacing of 0d at the Reynolds number of 1000. When the Reynolds number is 1100, the overall performance factor is 43% higher than that with a single rigid pillar. The vortices are periodically generated by the two pillars with the 5d spacing, and the disturbance to the boundary layer enhances the heat transfer downstream the region in the micro-channel.

Key words: *heat transfer enhancement, micro-channel, fluid-structure interaction, flexible vortex generator, dynamic mesh*

Introduction

Enhancement of convective heat transfer is required in many industrial applications. Micro-channel heat dissipation is a hot topic in recent studies. Various turbulence structures are applied in micro-channels to enhance fluid-flow disturbance and destroy the flow boundary-layer. Zhou *et al.* [1] studied heat transfer enhancements of pillars with different shapes in micro-channels both experimentally and numerically. Drop-shaped and irregular drop-shaped pillars increased the Nusselt number by 60-70%, but the pressure loss increased by 20-40%. Ahmed *et al.* [2] investigated the effect of micro-channel grooves on heat transfer performance. Four geometric parameters related to groove shape were considered to optimize the design for the micro-channel heat sink. Compared with the straight micro-channel at the Reynolds number of 100, the Nusselt number and the friction of the grooved micro-channel in-

* Corresponding author, e-mail: jin.wang@hebut.edu.cn

creased by 51.59% and 2.35%, respectively. Derakhshanpour *et al.* [3] numerically analyzed fluid-flow and heat transfer in micro-channels with semi-circular and semi-elliptic ribs. Results showed that the presence of the filleted corners resulted in a 22% increase in the performance evaluation criteria of micro-channels with semi-circular ribs. Lu and Zhai [4] proposed a combination of vortex generators (VG) and dimples in a micro-channel with a heat flux of 100 W/cm^2. In the Reynolds number range of 167-834, the heat transfer performance was improved by 23.4-59.8%, and the friction was increased by 22.1-54.4% compared with the smooth micro-channel. The liquid flow and conjugated heat transfer in micro-channels equipped with longitudinal vortex generators (LVG) were numerically investigated by Ebrahimi *et al.* [5]. Results showed that the Nusselt number of micro-channels with LVG increased by 2-25% for the Reynolds number in the range of 100-1100. Vinoth and Senthil [6] investigated the heat transfer performance of micro-channel heat sinks with various cross-sections. Results showed that the trapezoidal entrance section showed better comprehensive performance than the square and the semicircle sections. With the addition of nanoparticles, the heat transfer rate increased by 3.38% compared to the water on the trapezoidal cross-section. Wang *et al.* [7] proposed a combination scheme of micro-pin fins and vortex generators to improve heat transfer performance. The overall performance factor of the micro-channel with the combined structure was 9.6% and 5.4%, respectively higher than those with oval pillars and vortex generators. Ma *et al.* [8] investigated the effects of rolling conditions on the heat transfer performance of printed circuit heat exchangers. Results showed that the rolling condition had the most significant effect on the heat transfer of natural gas, and the maximum instantaneous Nusselt number increased by 40%. Lian *et al.* [9] found that the core volume of the composite printed circuit heat exchanger decreased by 49%, and the heat transfer rate per unit volume increased by 145% compared to the conventional printed circuit heat exchanger.

Nanoparticles are added to increase the thermal conductivity of base fluids. Ma *et al.* [10] summarized the research progress of nanofluids involved with machine learning methods. Anwar *et al.* [11] numerically investigated the effects of fin spacings on the thermal performance of 1.5% CuO-water nanofluids in mini-channel heat sinks. The temperature of the base fluid decreased by 9.1% using 0.2 mm fin spacing compared to deionized water. Siddiqui *et al.* [12] studied cooling rates of water-based Al_2O_3 and Cu nanofluids with 0.25% and 0.11% volume concentrations. With an increase in Reynolds number, Cu-water nanofluid showed better performance than Al_2O_3-water nanofluid. 12.56% increase in overall heat transfer coefficient was obtained for the Cu nanofluid. Fattahi [13] found a 150% increase in Nusselt number for 6% nanofluids compared to water. Dinarvand *et al.* [14] investigated the cooling capacity of Cu-water nanofluids in a magnetic field. As the Hartmann number increased in the range of 0 to 80, the local Nusselt number increased by 7.5%. Qomi *et al.* [15] studied the effect of pulsation velocity at the inlet on heat dissipation performance in micro-channels. When the Reynolds number increased from 100 to 500, the heat transfer performance was improved by 350%.

Many studies have shown that an elastic vortex generator (EVG) results in periodic vortex shedding to enhance the disturbance. The EVG obtains lower pressure loss than the rigid vortex generator (RVG). Hosseini *et al.* [16] investigated heat transfer enhancement in 2-D micro-channels with square obstacles and elastic beams. Results showed that the thermohydraulic performance factor of the elastic beam is 32% higher than that of the rigid beam. Lee *et al.* [17] studied a pair of symmetrically-arranged flexible fins in micro-channels. The flexible fins exhibited three moving modes, *i.e.*, flapping, fully deflected, and irregular modes. Flexible fins with the best parameters increased the thermal performance factor by 106%. Park *et al.* [18]

studied the effects of the inclination angle of a flexible wing on moving mode and flow field. When the inclination angle increased from 0.3π to 0.8π, the moving mode of the flexible wing changed from steady deflection to steady flapping. Chen *et al.* [19] enhanced fluid mixing in micro-channels with symmetrical and asymmetrical flexible wings. Results showed that the asymmetrical flexible wings had the highest comprehensive performance parameter of 1.44. Li *et al.* [20] arranged two freely rotatable pillars in the micro-channel. Results showed that the heat transfer performance of freely rotatable cylinders was 60% higher than that of stationary cylinders. Ali *et al.* [21] arranged flexible VG with an inclination angle of 30° on both sides of a channel. The global Nusselt number of the channel is 275% higher than that of the smooth channel. Shin *et al.* [22] processed pillars of aluminum and silicon composites. Due to the significant difference in thermal expansion rate between the two materials, the pillars deformed in the presence of a heat source. Results showed that the critical heat flux of the surface with the pillars was 10% higher than that of the conventional surface.

Few studies investigated effects of elastic pillars on heat transfer enhancement. In this research, two elastic pillars are arranged on the sides of the micro-channel. The elastic pillar shows higher Nusselt number and lower pressure loss than the rigid pillar. The heat transfer performance with different spacings of micropillars will be studied in detail. The mechanism of heat transfer enhancement is analyzed based on the displacement field of pillars and the vortex intensity in the micro-channel.

Description of geometry

Figure 1 shows a 2-D micro-channel model. A cylindrical obstacle is placed on the centerline of the micro-channel close to the inlet. Elastic pillars are arranged on two walls of the micro-channel. One end of a 2-D elastic pillar is fixed to the wall, and the other end is unrestricted. The dimensions of the computational model are given in tab. 1.

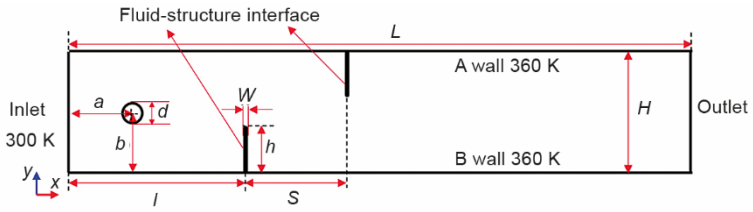

Figure 1. Computational model and nomenclature

The working fluid is deionized water and laminar and incompressible flow are assumed. The volumetric force of fluid acts on the elastic pillars, resulting in a bending deformation. The von-Mises stress within solid and the volumetric force exerted by fluid cause the elastic pillars to swing periodically. The spacing between pillars is set to 0, 5*d* and 10*d*.

Table 1. Model parameters

Parameters	Value	Parameters	Value
H	5*d*	*l*	10*d*
L	30*d*	*w*	0.16*d*
a	2.5*d*	*h*	2*d*
b	2.5*d*	*S*	0~10*d*
d	0.1 mm		

Mathematical formulation and numerical procedure

The ALE method is used to solve the continuity equation, fluid momentum equation, and heat transfer equation for this research. A dynamic mesh is added to the fluid-solid interface, and the mesh moving velocity appears in the governing equations from Donea *et al.* [23]:

$$\nabla U = 0 \tag{1}$$

$$\frac{\partial U}{\partial t} + [(U - U_g)\nabla]U = \nu\nabla^2 U - \frac{1}{\rho_\mathrm{f}}\nabla p \tag{2}$$

$$\frac{\partial T}{\partial t} + (U - U_g)\nabla T = \alpha\nabla^2 T \tag{3}$$

where U is the fluid velocity vector, U_g – the mesh velocity, p – the pressure, ρ_f – the fluid density, ν – the kinematic viscosity, t – the time, T – the temperature, and α – the thermal diffusivity.

The deformation and mechanics of the solid domain are computed by following equations from Tukovic *et al.* [24]:

$$\rho\mathrm{s}\frac{\partial^2 u}{\partial t^2} = \nabla(FS) \tag{4}$$

$$F = I + \nabla u \tag{5}$$

$$S = 2\frac{\partial W}{\partial C} \tag{6}$$

where u is the solid displacement, F – the deformation gradient tensor, S, I, W, and C – the second Piola-Kirchhoff stress tensor, the unity tensor, the strain energy density function, and the right Cauchy-Green deformation tensor, respectively.

$$W = \frac{1}{2}\mu(I_1^C - 3) - \mu\ln J + \frac{1}{2}\lambda(\ln J)^2 \tag{7}$$

$$\mu = \frac{E}{2(1+\nu)} \tag{8}$$

$$\lambda = \frac{\nu E}{(1+\nu)(1-2\nu)} \tag{9}$$

where I_1^C is the first invariant of C tensor and μ, λ are the Lame constants related to the elasticity modulus and Poisson ratio.

The software COMSOL Multiphysics 5.6 is used to solve the governing equations. Time integration is carried out with the backward differentiation formulae.

The equations are solved with an initial velocity $U(x, y, 0)$ of 0 m/s, initial pressure $P(x, y, 0)$ of 0 Pa, and initial temperature $T(x, y, 0)$ of 300 K. For a fully developed flow at the inlet of the micro-channel, a parabolic inlet velocity profile is:

$$U_\mathrm{inlet}(0, y, t) = \frac{3}{2}\overline{U}\left(\frac{4_y}{H^2}\right)(H - y) \tag{10}$$

where $\overline{U}$ is the mean velocity at the inlet and H – the height of micro-channel. The pressure at the outlet is set to 0 Pa. The Maxwell's slip condition is used for the velocity on the solid walls, Karniadakis *et al.* [25]:

$$U = U_{\mathrm{w}} + \sigma_{\mathrm{v}}\lambda\frac{\mathrm{d}Ux}{\mathrm{d}y} + \sigma_{\mathrm{T}}\nu\frac{\mathrm{d}}{\mathrm{d}x}(\ln T_{\mathrm{w}}) \tag{11}$$

where U_{w} (0 m/s) is the wall velocity, σ_{v} and σ_{T} are the viscous slip and temperature slip coefficients, which are defined:

$$\sigma_{\mathrm{v}} = \frac{2-\alpha_{\mathrm{v}}}{\alpha_{\mathrm{v}}} \tag{12}$$

$$\sigma_{\mathrm{T}} = \frac{3}{4} \tag{13}$$

The coefficient α_{v} denotes the tangential momentum accommodation coefficient (TMAC), indicating the portion of the incident molecules. It is 0.9 in the present research. The pressure at the outlet is set to 0. The inlet temperature of the fluid is 300 K. The outlet temperature is obtained by solving the equations. The temperature of the two walls is set constant, *i.e.,* 360 K. The circular obstacle is adiabatic. The density, thermal conductivity, and specific heat of the fluid are 998 kg/m, 0.6 W/mK, and 4200 J/kgK. The dynamic viscosity is given in tab. 2.

Table 2. Dynamic viscosity of DI-water

T [K]	μ [Pa·s]	T [K]	μ [Pa·s]	T [K]	μ [Pa·s]	T [K]	μ [Pa·s]
293	0.001 004	303	0.000 801 5	313	0.000 653 3	323	0.000 549 4
333	0.000 469 9	343	0.000 406 1	353	0.000 355 1	363	0.000 314 9

The connection between the elastic pillars and the walls is provided with a fixed constraint. The material of pillars is silicone rubber. Table 3 shows the mechanical properties of the material.

Table 3. Material properties of elastic pillars

Property	Value
Density	2500 kg/m^3
Elasticity modulus	4.5×10^6 Pa
Poison ratio	0.48
Thermal conductivity	2.5 W/mK
Specific heat	1200 J/kgK

Results and discussion

The model validation of this research involves a fluid-solid conjugate heat transfer problem. Figure 2(a) shows the time-average Nusselt number at two micro-channel walls with a single elastic pillar. The values and trends of the time-average Nusselt number agree with the results from [26]. Figure 2(b) shows the displacement fields of the elastic pillar tip in the x and y directions. It is observed that the amplitude and frequency of the elastic pillar vibration are consistent with the results from [26].

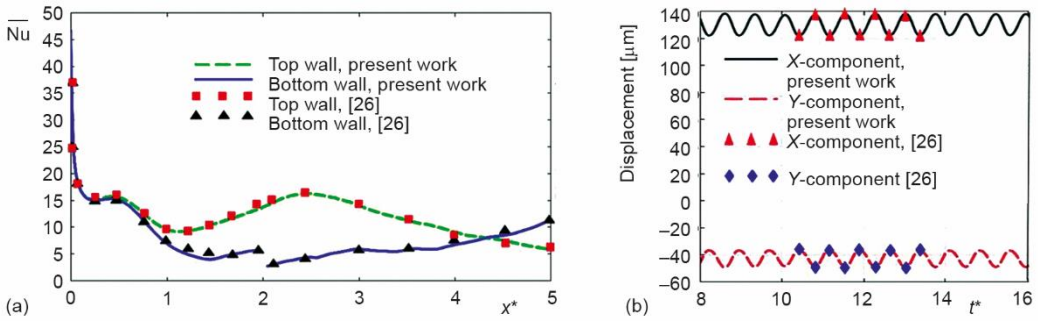

Figure 2. Comparisons of present research and published results; (a) time-average local Nusselt number and (b) displacement fields of the elastic pillar tip

The number of 760000 grids is used as a base case to conduct an analysis of grid independence as shown in tab. 4. When the number of grids is 420000, the error of the total Nusselt number is 0.3%. Considering the error below 1% and accepted computational time, the mesh with 420000 grids is selected for this study using a computer with eight processors (Intel Core i7-7700 CPU, 3.60 GHz, 8 GB RAM).

Table 4. Error and computation time corresponding to different mesh numbers

Number of meshes	Total Nusselt number	Errors	Computational time
80000	24.7	12.4%	1 hour and 9 minutes
180000	26.7	5.3%	2 hours and 34 minutes
420000	28.1	0.4%	8 hours and 14 minutes
760000	28.2	0%	17 hours and 3 minutes

Figure 3 shows the transient velocity fields for different spacings of pillars at the Reynolds number of 1000. When the spacing between two pillars is 0, the high-speed area is mainly located at the centerline of the micro-channel. The increase in blockage rate for the symmetrical channel allows the fluid to reach the maximum flow rate of 3 m/s compared to the other two asymmetrical channels. However, the velocity near the micro-channel walls is

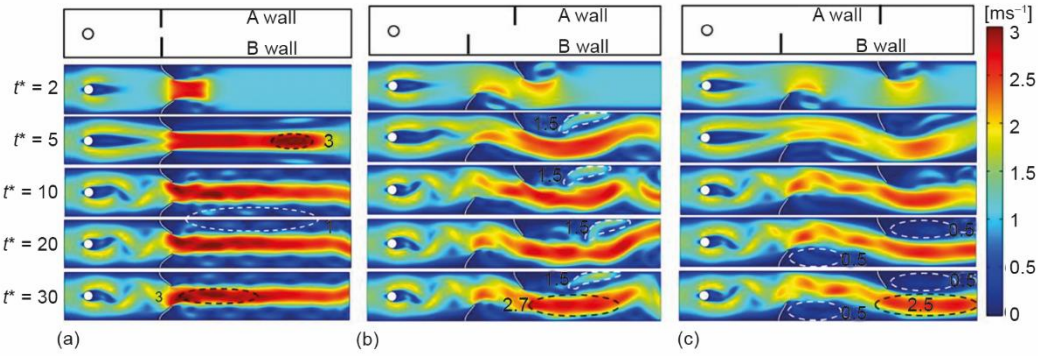

Figure 3. Transient velocity field for various spacing at Reynolds number of 1000; (a) no spacing (0), (b) spacing of 5*d*, and (c) spacing of 10*d*

less than 1 m/s. The asymmetric arrangement of two elastic pillars with a spacing of 0.5*d* causes a higher flow velocity close to the wall than the symmetric arrangement. The pillar on the A-wall drives the fluid towards the B-wall, but the local fluid velocity on the A-wall reaches 1.5 m/s. When the spacing between two pillars is 10*d*, the maximum velocity is 2.5 m/s after 30 seconds, corresponding to the lowest velocity among the three micro-channels. The fluid velocity is 0.5 m/s close to the walls downstream of two pillars. With the pillar spacing of 5*d*, the maximum velocity on the A-wall is observed in the region downstream the second pillar compared to the other arrangements especially after 5 seconds. This flow distribution enhances the convective heat transfer on the walls.

Figure 4 shows the temperature fields of the three micro-channels at the Reynold number of 1000. The initial temperature is set to 300 K. Two symmetrically arranged pillars alternate to create vortices to enhance the downstream fluid mixing. Multiple high temperature vortex cores are generated in the micro-channels with symmetrical and asymmetrical arrangements of pillars. The asymmetrical arrangement of elastic pillars creates disordered vortices, which further enhance fluid mixing. With a spacing of 5*d*, the fluid temperature near the free end of the pillar reaches 340 K, and the temperature near the fixed end of the pillar is 350 K. When the spacing of two pillars is 10*d*, the downstream region of the pillar on the A-wall has the highest temperature 340 K compared to the other two micro-channels. The convective heat transfer is weak due to the small temperature difference between the fluid and the wall.

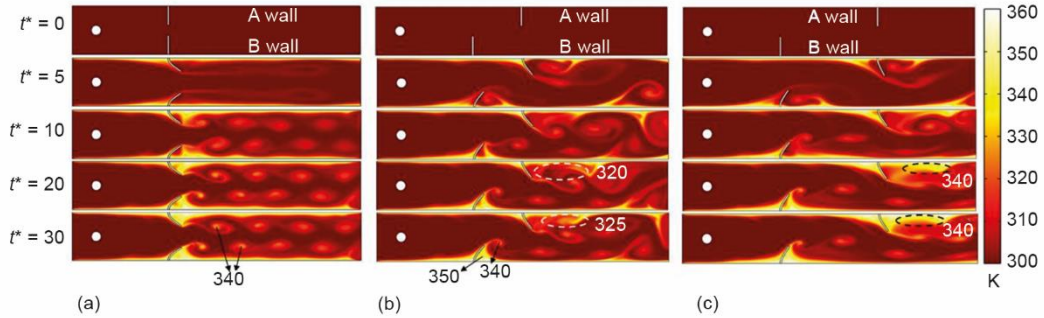

Figure 4. Transient temperature field for various spacing at Reynolds number of 1000; (a) no spacing (0), (b) spacing of 5*d*, and (c) spacing of 10*d*

Figure 5 shows displacements at the free end of the elastic pillars for Reynold snumber equal to 1000. Due to the formation of the Karman vortex and the swing of elastic pillars, the results are time-dependent. The dimensionless time is determined:

$$t^* = \frac{t\overline{U}}{H} \tag{14}$$

During the initial period, the pillars flex from a standing state. When dimensionless time is 8, the elastic pillars begin to oscillate periodically. Different spacings of pillars result in diverse amplitudes. When the spacing of pillars is 5*d*, the maximum displacements of the point-a in *X*-direction and *Y*-direction are 108 μm and 38 μm, respectively. The maximum displacements of point-b in the *X*-direction and *Y*-direction are 106 μm and 36 μm, respectively. When the spacing of pillars is 10*d*, the maximum displacements of point-a in the *X*-direction and in the *Y*-direction are 99 μm and 30 μm, respectively. During periodic oscillation, the

maximum displacements of point-b are 90μm in *X*-direction and 25 μm in *Y*-direction. For the elastic pillar on the B-wall, the maximum shape variation under the spacing of 10*d* is less than that under the spacing of 5*d*. In the periodic flapping process, the amplitude of the pillars on the B-wall with a spacing of 10*d* (15 μm) is slightly larger than that with a spacing of 5*d* (13 μm). The amplitude of the point-b is 2 μm in both *X*- and *Y*-directions, which is much smaller than the amplitude when the spacing is 5*d*.

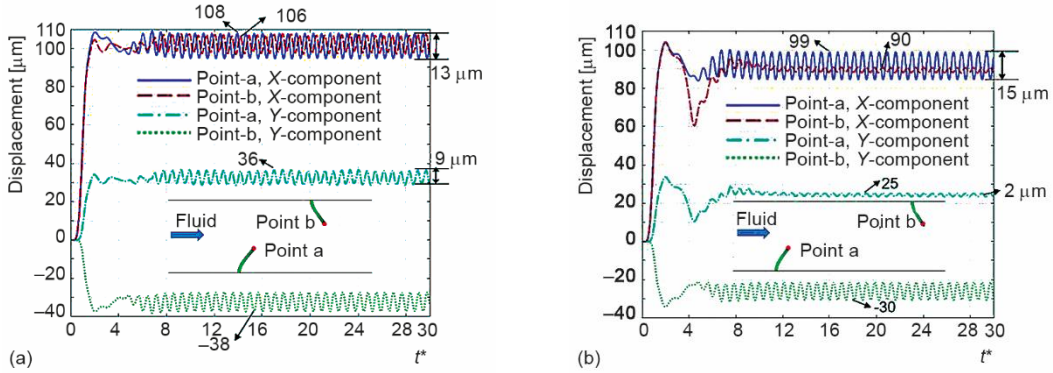

Figure 5. Displacements for the tip of elastic pillars at Reynolds number of 1000; (a) spacing of 5*d* and (b) spacing of 10*d*

Figure 6 shows the vortex intensity contours of the fluid-flow in micro-channels with various spacings of pillars at the Reynolds number of 1000. The swing of two symmetrically arranged pillars causes the vortex shedding alternately at the free end of elastic pillars. The maximum vortex intensity is about 18 1/s, but the flow separation of vortices is not conducive to the flow mixing. With the spacing of 5*d*, the vortices generated by the pillars on the two walls are sufficiently mixed in the downstream region, which will enhance the heat transfer efficiency. The mixing of vortices decreases the vortex intensity to 14 1/s. When the spacing between the two pillars is 10*d*, the vortex intensity is lower than that with 5*d* spacing of two pillars due to the amplitude 2 μm of the elastic pillar on the A-wall. The vortex intensity is 14 1/s downstream the pillars, and the vortices are difficult to mix together. The generation of vortices disturbs the boundary layer and promotes the mixing inside the fluid, improving the thermal efficiency of convective heat transfer.

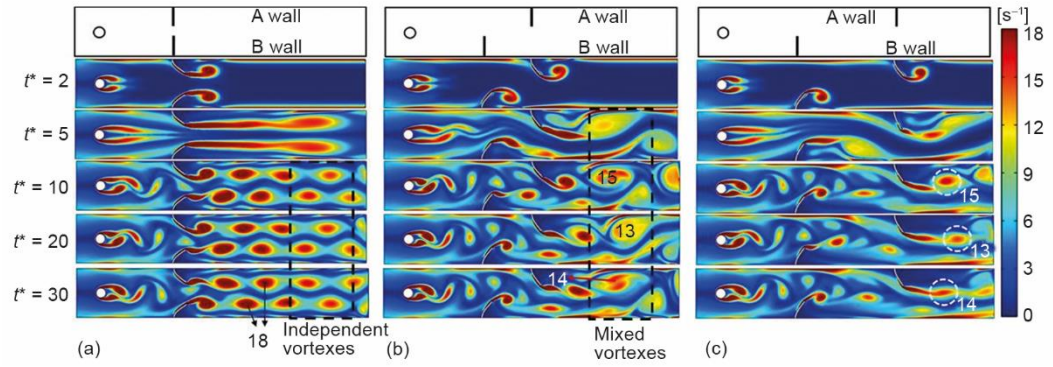

Figure 6. Vortex intensity for various spacings at Reynolds number of 1000; (a) no spacing (0), (b) spacing of 5*d* and (c) spacing of 10*d*

Figure 7 shows the time-average Nusselt number at different micro-channel walls under the Reynolds number of 1000. The x^* is the dimensionless length defined:

$$x^* = \frac{x}{H} \tag{15}$$

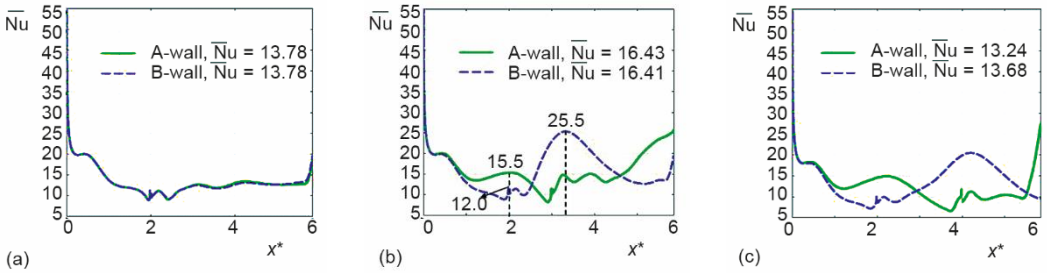

Figure 7. Time-average Nusselt number on the two walls at Reynolds number of 1000; (a) no spacing (0), (b) spacing of 5*d*, and (c) spacing of 10*d*

The Reynolds number based on the mean velocity at the channel inlet and the obstacle diameter is:

$$\mathrm{Re} = \frac{\rho \overline{U} d}{\mu} \tag{16}$$

The time-average Nusselt number, $\overline{\mathrm{Nu}}$, and the line-average Nusselt number, $\overline{\overline{\mathrm{Nu}}}$, are [27]:

$$\overline{\mathrm{Nu}}(x) = \frac{1}{t}\int_0^t \frac{q_\mathrm{w}(x,t)H}{k[T_\mathrm{w} - T_\mathrm{b}(x,t)]}\mathrm{d}t \tag{17}$$

$$\overline{\overline{\mathrm{Nu}}} = \frac{1}{L}\int_0^L \overline{\mathrm{Nu}}(x)\mathrm{d}x \tag{18}$$

where q_w is the average value of heat fluxes on the two walls, k – the thermal conductivity of the fluid, and T_b – the bulk temperature which is defined by:

$$T_\mathrm{b}(x,t) = \frac{\int_0^H U(x,y,t)T(x,y,t)\mathrm{d}y}{\int_0^H U(x,y,t)\mathrm{d}y} \tag{19}$$

The Nusselt number decreases with the increase in boundary-layer thickness close to the inlet. When the spacing of two pillars is 0, a symmetrical arrangement of pillars is obtained on the walls. The time-space average Nusselt numbers on the two walls are 13.78. For the spacing of 5*d*, the time-space average Nusselt number on the A-wall is 16.43, and that on the B-wall is 16.41. With the pillar spacing of 5*d*, the time-space average Nusselt number increases by 19.2% compared to that with no spacing. At position 3.5*H*, the local Nusselt number on the B-wall has a peak value of 25.5. The elastic pillar on the A-wall shows an effect on

fluid distribution close to the B-wall. At position 2*H*, The time-average Nusselt number on the A-wall is 15.5 which larger than that on B-wall (corresponding to 12.0). For the asymmetrical arrangement with the spacing of 10*d*, the line-average Nusselt number on the two walls are smaller than those with no spacing. The swing amplitude of the elastic pillar on the A-wall is 2 μm, which indicates that no fully-mixed fluid destroys the boundary-layer.

Figure 8 shows the pressure drop of different micro-channels. The symmetrically-arranged pillars create a small cross section of micro-channel, and the pressure drop is the maximum as compared to that of single elastic pillar, *S* of 10*d* and *S* of 5*d*. The pressure drop with 5*d* spacing is slightly larger than that of 10*d* spacing. Single elastic pillar creates a minimum blocking probability for the micro-channel, and the pressure drop is the lowest.

Figure 9 shows the variations of total Nusselt number and overall performance factor with Reynolds number in different micro-channels. The total Nusselt number is the sum of the time-space Nusselt number on the two walls. For all Reynolds numbers, the total Nusselt number with the spacing of 5*d* has the largest value of 33.06. The elastic pillars generate vortices in opposite directions, and the downstream mixing significantly improves the heat transfer efficiency. With no spacing, the total Nusselt number at a Reynolds number of 1000 is 27.56 and less than 28.54 at a Reynolds number of 900. The symmetrically arranged pillars make the fluid to concentrate in the central region of the micro-channel. The increase in flow rate deteriorates the heat transfer between fluid and the wall. The overall performance factor η is defined as:

$$\eta = \left(\frac{\mathrm{Nu_{tot}}}{\mathrm{Nu_0}}\right)\left(\frac{f}{f_0}\right)^{-\frac{1}{3}} \tag{20}$$

where the subscript 0 corresponds to the micro-channel with a rigid pillar and f – the friction factor:

$$f = \frac{2H}{L}\frac{\Delta P}{\rho \bar{U}^2} \tag{21}$$

In the Reynolds number range from 800 to 1100, the largest overall performance factor of 1.43 is obtained when the spacing of pillars is 5*d*. For the Reynolds number of 1100, the overall performance of the micro-channel with the pillar spacing of 5*d* is 43% higher than

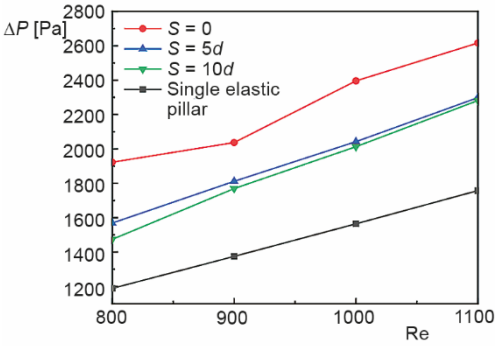

Figure 8. Pressure drops for different micro-channels

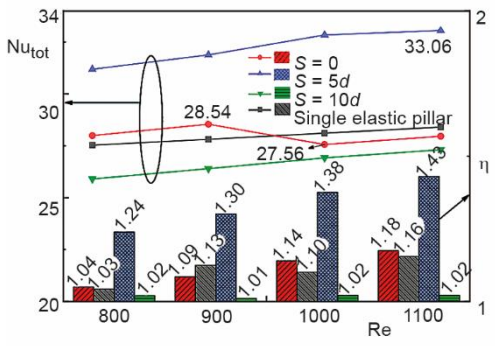

Figure 9. Total Nusselt number and overall performance factor of different micro-channels

that with a single rigid pillar. When the spacing is 10*d*, the overall performance factor is below 1.03 for all Reynolds number conditions. This result is because the amplitude of the elastic pillar on the A-wall is 2 μm, which has little effect on enhancing the heat transfer.

Conclusions

The effect of pillar spacing on heat transfer performance was studied in micro-channels numerically. The velocity, temperature, and displacement fields of elastic pillars were obtained by the ALE method. The time-averaged Nusselt number and overall performance factor were used to evaluate the heat transfer performance of different micro-channels. The main conclusions are as follows.

- Symmetrically-arranged elastic pillars oscillate alternately after flowing around a circular cylinder. Periodic vortex shedding occurs at the free end of the elastic pillars, but the mixing of vortices is limited by the spacing of pillars. When the Reynolds number is 1100, the overall performance factor of the micro-channel with symmetrically-arranged elastic pillars is 16% higher than that with the single rigid pillar.
- When the spacing of two pillars is 5*d*, the highest overall performance factor of 1.43 is obtained in the Reynolds number range of 800-1100. When the Reynolds number is 1100, the overall performance factor of two pillars with a distance of 5*d* is 43% higher than that of a single rigid pillar. The heat transfer efficiency in the downstream region is improved due to the mixing of vortices generated by the two elastic pillars.
- The micro-channel with the pillar spacing of 10*d* has a slight heat transfer enhancement. The overall performance factor increases by 2% compared to the micro-channel with a single rigid pillar.

The results of this study are mainly applied to the thermal management of microelectronic systems. Elastic pillars were arranged on the wall of the micro-channel, which improves the system efficiency. Compared with a rigid structure, the micro-channel with elastic pillars shows lower pressure loss. In addition, the results of this paper also provide methods for thermal management of batteries and solar photovoltaic systems.

Acknowledgment

This work is supported by the National Natural Science Foundation of China (Grant No. 52176067), the Science Fund for Distinguished Young Scholars of Hebei Province (Grant No. E2022202139), the Natural Science Foundation of Hebei Province of China (Grant No. E2021202163), and the Special Project of Science and Technology Winter Olympics in the Hebei Technology Innovation Guidance Plan (Grant No. 21474501D).

Nomenclature

C – right Cauchy-Green deformation tensor
F – deformation gradient tensor
f – friction coefficient
H – height of micro-channel, [μm]
I – unity tensor
I_I^C – first invariant of C tensor
Nu – Nusselt number
$\mathrm{Nu}_{\mathrm{tot}}$ – total Nusselt number
$\overline{\mathrm{Nu}}$ – time-average Nusselt number
$\overline{\overline{\mathrm{Nu}}}$ – line-average Nusselt number
p – pressure, [Pa]
Re – Reynolds number
S – second Piola-Kirchhoff stress tensor
T – temperature, [K]
T_b – bulk temperature of fluid, [K]
T_w – temperature of wall, [K]
t^* – dimensionless time
U – fluid velocity, [ms^{-1}]
U_g – mesh velocity, [ms^{-1}]
U_w – wall velocity, [ms^{-1}]
$\overline{U}$ – mean velocity at the inlet, [ms^{-1}]
u – solid displacement, [μm]
W – strain energy density function
x^* – dimensionless length

Greek symbols

α – thermal diffusivity, [m^2s^{-1}]
α_v – tangential momentum accommodation coefficient
ν – kinematic viscosity, [Pa·s]
η – overall performance factor
ρ_f – fluid density, [kgm^{-3}]
σ_v – viscous slip coefficients
σ_T – temperature slip coefficients

References

[1] Zhou, F., *et al.*, Experimental and Numerical Studies on Heat Transfer Enhancement of Micro-channel Heat Exchanger Embedded with Different Shape Micropillars, *Applied Thermal Engineering*, *175* (2020), July, 115296
[2] Ahmed, H. E., Ahmed, M. I., Optimum Thermal Design of Triangular, Trapezoidal and Rectangular Grooved Micro-channel Heat Sinks, *International Communications in Heat and Mass Transfer*, *66* (2015), Aug., pp. 47-57
[3] Derakhshanpour, K., *et al.*, Effect of Rib Shape and Fillet Radius on Thermal-Hydrodynamic Performance of Micro-channel Heat Sinks: A CFD Study, *International Communications in Heat and Mass Transfer*, *119* (2020), Dec., 104928
[4] Lu, G., Zhai, X., Analysis on Heat Transfer and Pressure Drop of a Micro-channel Heat Sink with Dimples and Vortex Generators, *International Journal of Thermal Sciences*, *145* (2019), Nov., 105986
[5] Ebrahimi, A., *et al.*, Numerical Study of Liquid Flow and Heat Transfer in Rectangular Micro-channel with Longitudinal Vortex Generators, *Applied Thermal Engineering*, *78* (2015), Mar., pp. 576-583
[6] Vinoth, R., Senthil, K., Numerical Study of Inlet Cross-Section Effect on Oblique Finned Micro-channel Heat Sink, *Thermal Science*, *22* (2018), 6B, pp. 2747-2757
[7] Wang, J., *et al.*, Effects of Pin Fins and Vortex Generators on Thermal Performance in a Micro-channel with Al_2O_3 Nanofluids, *Energy*, *239* (2022), Jan., 122606
[8] Ma, T., *et al.*, Thermal-Hydraulic Characteristics of Printed Circuit Heat Exchanger Used for Floating Natural Gas Liquefaction, *Renewable and Sustainable Energy Reviews*, *137* (2021), Mar., 110606
[9] Lian, J., *et al.*, Thermal and Mechanical Performance of a Hybrid Printed Circuit Heat Exchanger Used for Supercritical Carbon Dioxide Brayton Cycle, *Energy Conversion and Management*, *245* (2021), Oct., 114573
[10] Ma, T., *et al.*, Recent Trends on Nanofluid Heat Transfer Machine Learning Research Applied to Renewable Energy, *Renewable and Sustainable Energy Reviews*, *138* (2021), Mar., 110494
[11] Anwar, M., *et al.*, Numerical Study for Heat Transfer Enhancement Using CuO Water Nanofluids through Mini-Channel Heat Sinks for Microprocessor Cooling, *Thermal Science*, *24* (2020), 5A, pp. 2965-2976
[12] Siddiqui, A., *et al.*, Evaluation of Nanofluids Performance for Simulated Microprocessor, *Thermal Science*, *21* (2017), 5, pp. 2227-2236
[13] Fattahi, A., LBM Simulation of Thermo-Hydrodynamic and Irreversibility Characteristics of a Nanofluid in Micro-channel Heat Sink under Affecting a Magnetic Field, *Energy Sources, Part A: Recovery, Utilization, and Environmental Effects*, On-line first, https://doi.org/10.1080/15567036.2020.1800868, 2020
[14] Dinarvand, M., *et al.*, Cooling Capacity of Magnetic Nanofluid in Presence of Magnetic Field Based on First and Second Laws of Thermodynamics Analysis, *Energy Sources, Part A: Recovery, Utilization, and Environmental Effects*, *44* (2022), pp. 7825-7840
[15] Qomi, *et al.*, A., 2020, Heat Transfer Enhancement in a Micro-channel Using a Pulsating MHD Hybrid Nanofluid-flow, *Energy Sources, Part A: Recovery, Utilization, and Environmental Effects*, on-line first, https://doi.org/10.1080/15567036.2020.1834031, 2020
[16] Hosseini, S., *et al.*, An Immersed Boundary-Lattice Boltzmann Method with Multi Relaxation Time for Solving Flow-Induced Vibrations of an Elastic Vortex Generator and Its Effect on Heat Transfer and Mixing, *Chemical Engineering Journal*, *405* (2021), Feb., 126652
[17] Lee, J. B., *et al.*, Heat Transfer Enhancement by Flexible Flags Clamped Vertically in a Poiseuille Channel Flow, *International Journal of Heat and Mass Transfer*, *107* (2017), Apr., pp. 391-402
[18] Park, S. G., Heat Transfer Enhancement by a Wall-Mounted Flexible Vortex Generator with an Inclination Angle, *International Journal of Heat and Mass Transfer*, *148* (2020), Feb., 119053
[19] Chen, Y., *et al.*, Heat Transfer Enhancement in a Poiseuille Channel Flow by Using Multiple Wall-Mounted Flexible Flags, *International Journal of Heat and Mass Transfer*, *163* (2020), Dec., pp. 120447

[20] Li, L., *et al.*, Enhancement of Heat Transfer and Mixing with Two Side-by-Side Freely Rotatable Cylinders in Micro-channel, *International Journal of Heat and Mass Transfer*, *189* (2022), June, 122717
[21] Ali, S., *et al.*, Heat Transfer and Mixing Enhancement by Using Multiple Freely Oscillating Flexible Vortex Generators, *Applied Thermal Engineering*, *105* (2016), July, pp. 276-289
[22] Shin, S., *et al.*, Enhanced Boiling Heat Transfer Using Self-Actuated Nanobimorphs, *Nano Letters*, *18* (2018), 10, pp. 6392-6396
[23] Donea, J., *et al.*, Arbitrary Lagrangian-Eulerian Methods, in: *Encyclopedia of Computational Mechanics,* John Willy and Sons, New York, USA, 2004, Chapter 14, pp. 1-25
[24] Tuković, Ž., Jasak, H., Updated Lagrangian Finite Volume Solver for Large Deformation Dynamic Response of Elastic Body, *Transactions of Famena*, *31* (2017), 1, Chapter 14, pp. 55-70
[25] Karniadakis, G. E., *et al.*, Microflows and Nanoflows: Fundamentals and Simulation, in: *Interdisciplinary Applied Mathematics,* Springer, New York, USA, 2006, Vol. 29
[26] Dadvand, A., *et al.*, Enhancement of Heat and Mass Transfer in a Micro-channel via Passive Oscillation of a Flexible Vortex Generator, *Chemical Engineering Science*, *207* (2019), Nov., pp. 556-580
[27] Celik, I. B., *et al.*, Procedure for Estimation and Reporting of Uncertainty Due to Discretization in CFD Applications, *Journal of Fluids Engineering*, *130* (2008), 7, 078001

Paper submitted: June 17, 2022
Paper revised: August 16, 2022
Paper accepted: August 18, 2022